Assessing total water storage and identifying flood events over Tonlé Sap basin in Cambodia using GRACE and MODIS satellite observations combined with hydrological models

Tangdamrongsub, N.; Ditmar, P. G.; Steele-Dunne, S. C.; Gunter, B. C.; Sutanudjaja, E. H.

DOI
10.1016/j.rse.2016.03.030

Publication date
2016

Document Version
Accepted author manuscript

Published in
Remote Sensing of Environment: an interdisciplinary journal

Assessing total water storage and identifying flood events over Tonlé Sap basin in Cambodia using GRACE and MODIS satellite observations combined with hydrological models

N. Tangdamrongsub[a*], P. G. Ditmar[a], S. C. Steele-Dunne[b], B. C. Gunter[a,c], E. H. Sutanudjaja[d]

[a] Department of Geoscience and Remote Sensing, Faculty of Civil Engineering and Geosciences, Delft University of Technology, Delft, The Netherlands

[b] Department of Water Resources, Faculty of Civil Engineering and Geosciences, Delft University of Technology, Delft, The Netherlands

[c] School of Aerospace Engineering, Georgia Institute of Technology, Atlanta, The United States of America

[d] Department of Physical Geography, Faculty of Geosciences, Utrecht University, Utrecht, The Netherlands

Corresponding author*: N. Tangdamrongsub (N.Tangdamrongsub@tudelft.nl)

Abstract

In this study, satellite observations including gravity (GRACE), terrestrial reflectance (MODIS), and global precipitation (TRMM) data, along with the output from the PCR-GLOBWB hydrological model, are used to generate monthly and sub-monthly terrestrial water storage (TWS) estimates and quantify flood events over the Tonlé Sap basin between 2002 and 2014. This study is the first time GRACE data have been used to investigate the hydrological processes over the Tonlé Sap basin. To improve the accuracy of the TWS estimates from GRACE, a signal restoration method was applied in an effort to recover the signal loss (i.e., signal leakage) inherent in the standard GRACE post-processing scheme. The

method applies the correction based on the GRACE observations only, requiring no external data or hydrological models. The effectiveness of the technique over the Tonlé Sap basin was validated against several independent data sets. Based on the GRACE observations since 2002, the 2011 and 2013 flood events were clearly identified, and measured to have basin-averaged TWS values of 42 cm (40% higher than the long-term mean peak value) and 36 cm (34% higher) equivalent water height, respectively. Those same years also coincide with the largest observed flood extents, estimated from the MODIS data as 6,561 km^2 (91% above the long-term mean peak value) and 5,710 km^2 (66% above), respectively. Those flood events are also linked to the observed inter-annual variations of water storage between 2010 and 2014. It was shown that those inter-annual variations mainly reflect the variations in the surface water and groundwater storage components, influenced by the change of the precipitation intensity. In addition, this study presents a new approach for deriving monthly and sub-monthly TWS variations over a regularly inundated area by using MODIS reflectance data in addition to GRACE solutions. The results of this study show that GRACE data can be considered as an effective tool for monitoring certain small-scale (82,000 km^2) hydrological basins.

Keywords: GRACE, MODIS, TWS, Tonlé Sap, signal restoration, inundation area, PCR-GLOBWB

1. Introduction

The main goal of this study is to quantify flood events in the Tonlé Sap basin in Central Cambodia at both basin and sub-basin scales. It is shown that a combination of several satellite data products in this data-sparse region can yield valuable insight into flood pulses during the last 15 years.

The Tonlé Sap basin has an area of approximately 82,000 km^2 and contains the largest freshwater lake (Tonlé Sap Lake) in Southeast Asia, which serves as the primary fresh water resource for various food and agricultural activities of Cambodia (Lamberts, 2001). Apart from precipitation, the Tonlé Sap Lake regularly receives water from the Mekong River through the Tonlé Sap River. In addition, the Mekong

River brings sediment and nutrients to the soil, making the Tonlé Sap basin favorable for fisheries and the cultivation of rice and other crops. The agricultural activities in the Tonlé Sap basin require irrigation, and the irrigated area has been expanded in the past decade in line with the implementation of a national strategic plan (Yu and Diao, 2011). This has facilitated agriculture growth in the area, so that now more than half of the Cambodian rice fields are located within the basin. Importantly, several new hydro-electric power plants have been constructed in the regions upstream of the Mekong River (outside Cambodia). These developments have altered the natural flows of Mekong mainstream, which has a direct impact to on the Tonlé Sap water level (Arias et al., 2012; Kummu et al., 2014; Cochrane et al., 2014). Compounded by climate variability, the frequency and intensity of drought and flood events in the region have become more severe and have led to the destruction of irrigation fields and civilian casualties (NCDM and UNDP, 2015). It is clear that for the development and prosperity of all of the countries dependent on the Mekong and Tonlé Sap basins, improved long-term monitoring of the region's water resources is needed. Such monitoring will serve inter-governmental agencies like the Mekong River Commission (MRC), which aim to optimize the usage of water resources during the country's development while minimizing the harmful effects on people and the environment of the region. Despite the clear need for hydrological information, the vast and inaccessible nature of the Tonlé Sap area makes it difficult to collect in situ observations. As a result, remote sensing observations have to be exploited. This study is a first attempt to provide a comprehensive assessment of the large-scale variations of the water storage as well as to explore flood events in the Tonlé Sap basin over the past decade, using various data sets delivered by remote sensing satellites.

In several studies in the past, terrestrial surface reflectance data have been used to identify the spatial flooding patterns over the Tonlé Sap Lake (Xiao et al., 2005; Sakamoto et al., 2007; Arias et al., 2012). However, that analysis did not allow the total water storage variations to be accurately quantified. To address this issue, data from the Gravity Recovery And Climate Experiment (GRACE) satellite mission (Tapley et al., 2004) are used in our study. In contrast to the terrestrial surface reflectance observations,

GRACE senses the total Terrestrial Water Storage (TWS) variations in all components (e.g., surface water, soil moisture, and groundwater) (Bettadpur, 2012). For this reason, GRACE data have been used in many hydrological applications at both global and regional scales, e.g., groundwater depletion in India (Rodell et al., 2009), flood prediction for Mississippi River basin (Reager et al., 2014) and characterization of regional (e.g., Amazon, Zambezi, Texas) drought signatures (Thomas et al., 2014). However, to date GRACE data have never been applied to study hydrological processes over the Tonlé Sap basin. The results based on GRACE data are supported and validated by means of other satellite remote sensing datasets and hydrological models.

One of the challenges in using GRACE data is their temporal resolution, which is limited to one month, as well as their coarse spatial resolution (typically > 300 km). Unconstrained GRACE products require the application of some form of spatial filtering to reduce the effects of high-frequency errors inherent to the publicly available GRACE fields. This spatial filtering redistributes the signal over the filter radius, commonly referred to as signal leakage, requiring additional processing to restore this leaked signal if accurate TWS results over a specific target area are desired. Several signal restoration methods have been described in the literature for this purpose. Landerer and Swenson (2012) applied a scaling factor computed as the ratio between the true TWS and filtered TWS, based on a hydrological model. The procedure is simple but may introduce a bias caused by the dependency on a particular hydrological model. Baur et al. (2009) applied a correction based on known signal geometry. Their method was developed to restore the signal along the coastal zone of Greenland. The method does not rely on external data and can be very effective, but requires a controlled environment, where the surrounding signal is smaller than the target one, and the signal location is known. More recently, Chen et al. (2013, 2014) proposed a strategy similar to that of Baur et al. (2009) but without the known signal geometry requirement. The main idea is to mitigate the leakage out signal (from land to ocean) using GRACE data directly, so that the signal damping effect near the coast is effectively reduced (Chen et al., 2013). This strategy is straightforward, easy to implement, and has been proven effective for inland applications (Chen et al., 2014). As will be

shown later, the results produced compared well with independent validation data, suggesting the approach is suitable for this study as well.

Apart from GRACE observations, precipitation data from the Tropical Rainfall Measuring Mission (TRMM, Kummerow et al., 1998), as well as three hydrological models are used in an attempt to better understand the processes responsible for the observed TWS variations. The hydrological models used are: (i) the Centre for Medium-Range Weather Forecasts (ECMWF) ReAnalysis-Interim (ERA-Interim) Full Resolution (Dee, 2011); (ii) the Global Land Data Assimilation System (GLDAS; Rodell et al., 2004); and (iii) the PCRaster Global Water Balance (PCR-GLOBWB) (Van Beek et al., 2011; Sutanudjaja et al., 2014; Wada et al., 2014). In contrast to the ERA-Interim and GLDAS models that construct TWS based on soil moisture storage, the PCR-GLOBWB model also contains surface water and groundwater storage components and can be used to distinguish the contribution of different storage components to the TWS.

Furthermore, the coarse temporal and spatial resolution of GRACE requires supporting information to cover smaller temporal and spatial scales. This information is obtained from the terrestrial surface reflectance data provided by the Moderate-Resolution Imaging Spectroradiometer (MODIS; Vermote et al., 2011), which form images with a spatial resolution of 500 m every 8 days. To distinguish the open water from soil and vegetation, the Normalized Different Water Index (NDWI; McFeeters, 1996) is used. In the first instance, NDWI data are used to quantify variations of the inundated area, which is essential for flood area planning. However, by using an empirical relationship between GRACE (TWS) and MODIS (NDWI-based) data over the inundated area, it is also possible to estimate the TWS variations from the MODIS data. This is important because it enables the estimation of TWS variations at sub-monthly time scales. To the author's knowledge, this is the first time that TWS variations have been produced from MODIS data.

This paper begins with an overview of the Tonlé Sap basin, given in Sect. 2. The description of all data and their processing are presented in Sect. 3. The GRACE signal restoration scheme is described in Sect. 4.

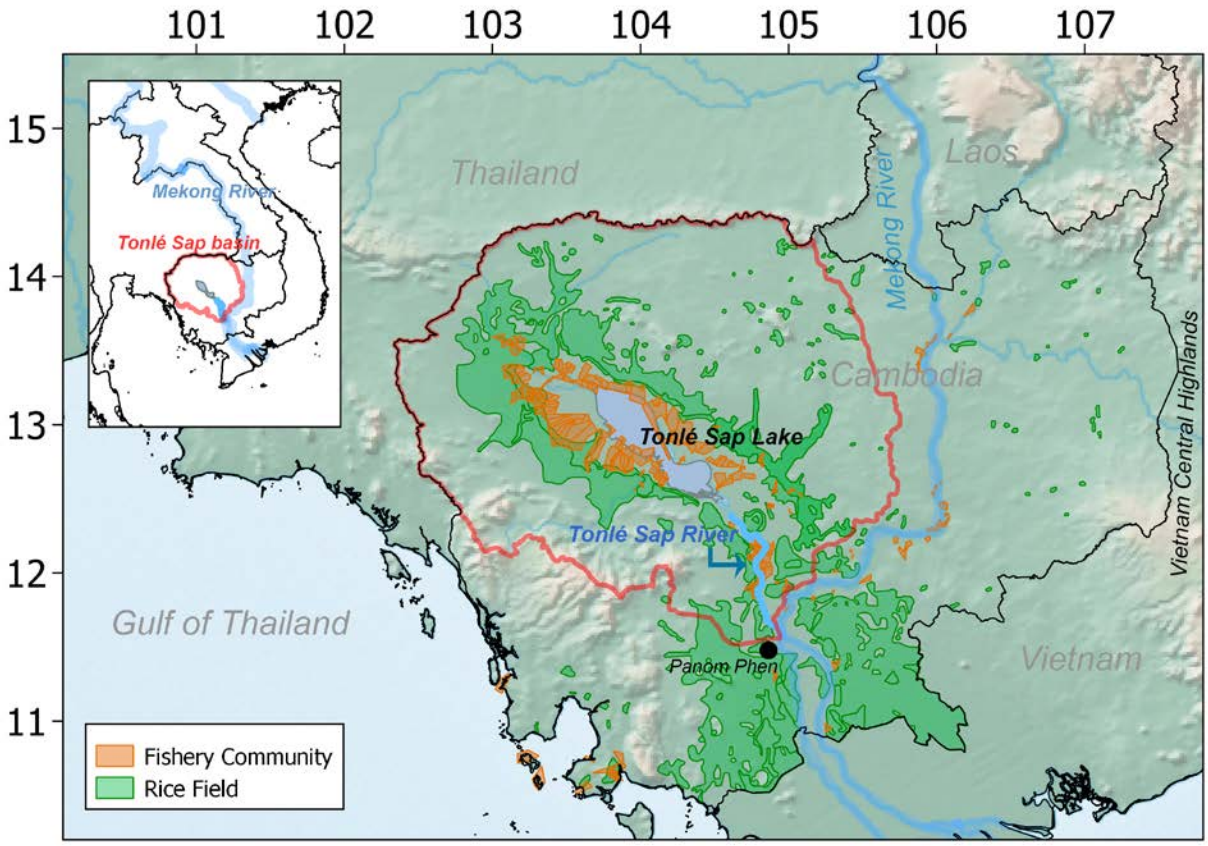

Fig. 1: Geographical location of the Tonlé Sap basin (red line). The shapefiles of the Tonlé Sap basin, Tonlé Sap Lake, fishery community and rice field were obtained from the Open Development Cambodia website (http://www.opendevelopmentcambodia.net/maps/downloads).

Sect. 5 focuses on the results obtained. The performance of the signal restoration method, as well as of the hydrological models, is evaluated in Sect. 5.1. Precipitation is analyzed in Sect. 5.2. In Sect. 5.3, we demonstrate the usage of MODIS data to estimate the TWS variations over the Tonlé Sap Lake floodplain. Sect. 5.4 is focused on the investigation of the inter-annual signal over the Tonlé Sap basin. Finally, Sect. 6 discusses and summarizes the main results of the study.

2. Study region

The Tonlé Sap basin extends over eight major Cambodian provinces and occupies approximately 46% of the land area of Cambodia. Tonlé Sap Lake (Fig. 1) located in the center part of the basin has an area in the dry and wet seasons of approximately 2,500 km^2 and 16,000 km^2, respectively (Lim et al., 1999). The region has a monsoon climate, which is characterized by a rainy period between May and October and a dry period between November and April, with an average rainfall of approximately 1,750 mm/year. Under normal conditions, the lake releases water through the Tonlé Sap River, which connects to the Mekong River near Panom Phen. However, in a wet season (when the amount of rainfall by far exceeds the average level), the lake receives the return flow water from the Mekong River leading to flooding over the Tonlé Sap Lake floodplain. The flood extent is particularly large when the Tonlé Sap basin (and Mekong river basin) experiences a high level of rainfall from strong tropical cyclones (e.g., Typhoon Nesat and Nalgae in 2011, Typhoon Haiyan in 2013).

3. Data and data processing

3.1 GRACE

In this study, the GRACE CSR-Release05 monthly gravity field products from April 2002 to October 2014 were used. These fields were produced at the University of Texas at Austin, Center for Space Research (CSR) (Bettadpur, 2012). The products come in the form of spherical harmonic coefficients (SHC) up to degree and order 60, corresponding to a (half-wavelength) spatial resolution of approximately 330 km). The degree-1 coefficients are provided by Swenson et al. (2008). Because of large uncertainties in the degree-2 coefficients of the GRACE solutions, the values obtained by satellite laser ranging (Cheng and Tapley, 2004) are used instead. In the months without GRACE gravity solutions (e.g., June and July 2003, June 2004), the SHC values were calculated using a cubic-spline interpolation. Then, the long-term

mean of the SHC (between April 2002 and October 2014) was computed and removed from each monthly SHC to obtain the monthly variations of the gravity field.

Next, high-degree errors were alleviated by using de-striping (Swenson and Wahr, 2006) and Gaussian smoothing (Jekeli, 1981) filters. The parameters of de-striping filter used in this study were similar to those discussed in Duan et al. (2009) (A=30, K=10 in equation (1)). A polynomial of degree 2 was used, and the orders lower than 5 were kept unchanged. The radius (R) of the Gaussian smoothing filter was 350 km. After filtering, the SHCs were converted to the 0.5-degree gridded TWS variations over the Tonlé Sap basin. The effects of post-glacial rebound (Peltier, 2004) over the study area are negligibly small, so no correction was made for them.

3.2 Hydrological models

Three hydrology models were used in this study, and the definition of TWS varied depending on the storage components considered in each of the models:

1. GLDAS-NOAH Version 1: Monthly one-degree nearly-global gridded data are provided for different storage components separately. The TWS was constructed as the sum over all available components, i.e., four soil moisture layers: 0–10, 10–100, 100–150, and 150–200 cm, and the total canopy water storage. Note that contribution of the total canopy water storage is minor (<1%) over the Tonlé Sap basin.
2. ERA-Interim Full Resolution: The reanalysis volumetric soil moisture from the ECMWF is available every 6 hours at approximately 80-km spatial resolution. The volumetric soil moisture was converted to equivalent water height by multiplying by the thickness of the layer. Similar to GLDAS, TWS was computed as the sum over 4 soil moisture layers: 0–7, 7–28, 28–100, and 100–289 cm. The monthly TWS was then computed by averaging the 6-hour data over the month.

3. PCR-GLOBWB Version 2.0: daily 0.5-degree TWS estimates are provided globally as the sum of 7 water storage components: snow, interception, river channels (including lakes), irrigation, upper soil moisture (0–30 cm depth from the surface), lower soil moisture (30–150 cm depth), and groundwater. The monthly TWS was computed by averaging the daily data of the month. A further description of PCR-GLOBWB can be found in Appendix A.

The monthly TWS values from all 3 models were constructed for the time interval between April 2002 and October 2014. For every model, the long-term mean of the TWS was computed and removed from each monthly estimate to obtain the TWS variation consistent with the one derived from GRACE data.

3.3 MODIS-derived NDWI

The MODIS sensors on board NASA's Terra and AQUA satellites have been successfully collecting spectral imaging data for more than a decade. Among more than 20 product types, the MODIS Surface-Reflectance Product (MOD 09) provides the surface reflectance in 7 different frequency bands every 8 days (Vermote et al., 2011). Combinations of specific frequency bands can be used to identify open water bodies of the size of approximately 500 m and more (MOD 09 spatial resolution). Therefore, it is possible to calculate the variations of the inundated area of the Tonlé Sap Lake from this product. In this study, the NDWI derived from MYD09A1 (AQUA) product was used. The surface reflectance in different frequency bands was extracted from the MODIS tile h28v07 (covering the floodplain of the Tonlé Sap Lake). Based on the data quality control information, the pixels flagged with cloud cover or fill values were masked. The NDWI was computed based on reflectance from green and near infrared (NIR) channels as follows:

$$NDWI = (green - NIR)/(green + NIR). \quad (1)$$

The range of NDWI is between -1 and 1. Positive NDWI values represent the open water while the zero or

203 negative values represent soil and terrestrial vegetation (McFeeters 1996). Due to the limited data
204 availability, NDWI was computed starting from July 2002.

205 ### 3.4 Precipitation

206 Precipitation data were obtained from TRMM (Kummerow et al., 1998), a joint NASA/JAXA mission.
207 Several sensors (e.g., radar, microwave, infrared) were used to collect the precipitation-related passive
208 microwave data, which contain the hydrometeor profiles information. In this study, the latest released
209 monthly precipitation data (TRMM 3B43 Version 7; Huffman et al., 2007) between April 2002 and
210 October 2014 were used. The product provides the rainfall estimates every 0.25 degree between 50^{o} S and
211 50^{o} N.

212

213 ## 4. GRACE signal restoration methodology

214 The GRACE inter-satellite range observable does not measure TWS variations directly, and requires
215 processing to relate the absolute and relative accelerations of the twin satellites to variations in the gravity
216 field. The publicly available GRACE SHC products contain high-frequency errors that require the use of a
217 spatial filter to suppress them. As mentioned earlier, both signal and error are impacted by this filtering
218 step, making restoration of the leaked signal important for proper characterization of the full TWS
219 changes in the basin. Similar to the approach of Chen et al. (2014), the following signal restoration
220 scheme is applied (see also Fig. 2):

221 1. After de-striping and Gaussian filtering are applied to the GRACE SHC (result from Sect. 3.1),
222 the TWS variation in the form of Equivalent Water Height (EWH) is computed following Wahr
223 et al. (1998). The result is set as the filtered reference TWS.
224 2. A candidate TWS variation (i.e., the "candidate TWS") is introduced and is set equal to the
225 filtered reference TWS.

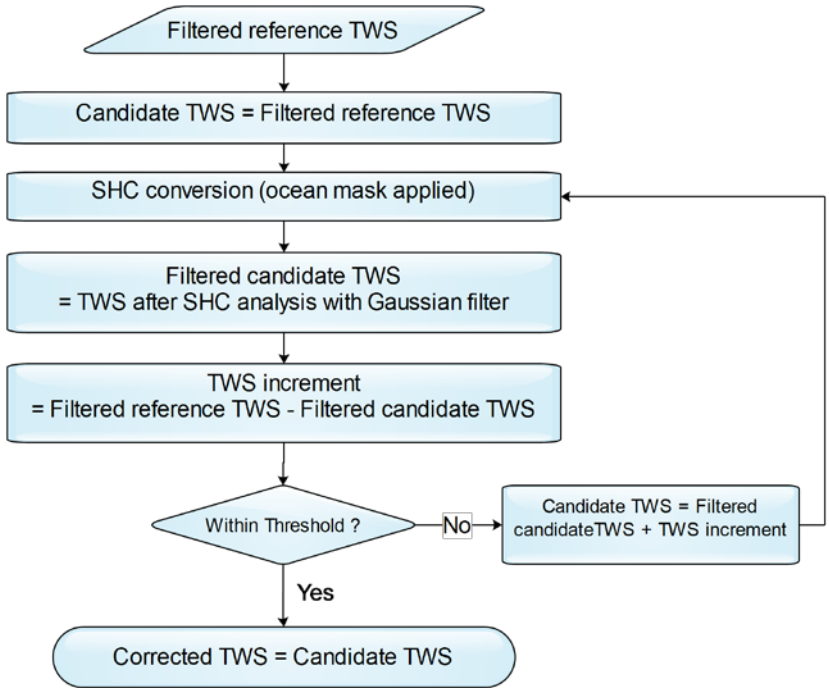

Fig. 2: Flowchart of the GRACE signal restoration scheme

3. The candidate TWS is set equal to zero over the oceans. After that, it is converted to SHCs up to degree 60, with a Gaussian filter of radius R=350 km applied. Then, the SHCs are converted back to TWS variations. Note that, following the recommendation of Chen et al. (2014), the de-striping filter is not applied. The result of this step is called the "filtered candidate TWS".
4. The TWS increment is computed as the filtered reference TWS minus the filtered candidate TWS.
5. If the TWS increment satisfies a stopping criterion (e.g., if the difference in every grid cell is smaller than a pre-defined threshold), the candidate TWS is defined as the corrected TWS (the final product). Otherwise, the candidate TWS is updated by adding the TWS increment and the steps 3–5 are repeated.

It is emphasized here that the signal restoration process was applied to the TWS globally, but the stopping criterion was locally defined. The stopping criterion was chosen empirically: the signal restoration process was repeated until the increment TWS in every grid cell inside the Tonlé Sap basin became smaller than

241 0.5 cm EWH. Note that the selected value is 3–4 times smaller than the noise level of TWS variations
242 derived from GRACE (Wahr et al., 2006; Klees et al., 2008; Dahle et al., 2014). For all monthly solutions,
243 the criterion was met after about 30–40 iterations.

244 To study the sensitivity of the obtained results to the choice of the Gaussian filter radius, four more time
245 series of the corrected TWSs were computed using the same signal restoration procedure but with other
246 Gaussian filters radii R: 300, 400, 450, and 500 km. Every month, the error bounds were drawn based on
247 the minimum and maximum values taken from the 5 time series (including the case of R=350 km).

248 Furthermore, two more variants of the corrected TWS were produced for comparison.

249 1. To evaluate the sensitivity of the signal restoration method to the choice of the filter radius, the
250 filtered land mass data provided by the GRACE Tellus website were considered
251 (http://grace.jpl.nasa.gov; last access: 24 March 2015). Similar to this study, the land mass grid
252 data (CSR option) were also produced using the CSR RL05 product, but using different de-
253 striping parameters, and with the Gaussian smoothing radius set equal to 300 km (see
254 http://grace.jpl.nasa.gov/data/gracemonthlymassgridsland; last access: 24 March 2015). The filter
255 radius R in the signal restoration procedure was defined consistently. For clarity, the term
256 "GRACE TWS" is used below to represent the results of the processing from this study (Sect. 3.1)
257 while the term "GRACE TWS (Tellus)" is used to represent the results based on the data obtained
258 from the Tellus website.
259 2. To compare the performance of the signal restoration method and the scale parameter method
260 (Landerer and Swenson, 2012), the latter technique was used to post-process the filtered TWS
261 instead. The scale parameters were computed based on the three hydrological models considered
262 in our study. First, the original monthly TWS variations from each hydrological model were
263 converted to the SHCs, and the SHCs were Gaussian filtered using the same smoothing radius as
264 in the case of GRACE (350 km, see Sect. 3.1). The filtered SHCs were then converted to TWS
265 (called the filtered TWS). Second, the time-series of mean TWS over the Tonlé Sap basin was

computed from the filtered TWS and the original TWS, and the former was fit using least-squares to the latter using one scale parameter. The scale parameters estimated from GLDAS-NOAH, ERA-Interim, and PCR-GLOBWB hydrology models were 1.63, 1.27, and 1.67, respectively. The difference in the estimated values was likely influenced by the model dependency. As indicated by Landerer and Swenson (2012), the estimated scale parameter over the small river basin could be biased toward the hydrology model applied. Therefore, instead of applying the scale parameter individually, the mean value of 1.52 was used to scale the filtered TWS extracted from GRACE.

5. Results

5.1 TWS variations estimated over the Tonlé Sap basin

5.1.1 Signal restoration from the filtered GRACE-based estimates

The signal restoration method was applied to the filtered monthly GRACE TWS variations. The results before and after the restoration are demonstrated in Fig. 3 for the flood months of October 2009, 2011, and 2013. Before the signal restoration, a single maximum was observed in the northern part of the basin with the amplitude reaching approximately 10 – 20 cm EWH (Fig. 3 (a,b,c)). After the restoration, the TWS variations between the Tonlé Sap basin and Central Highlands of Vietnam became apparent in all solutions (see Fig. 3 (d,e,f)), and TWS amplitude reached approximately 40-45 cm EWH (see contours in Fig. 3 (d,e,f)). As the signal restoration process was designed without any involvement of the hydrology model or any other external data, the agreement with an independent hydrological model provides some confidence in the GRACE TWS estimates. The TWSs derived from PCR-GLOBWB hydrological model were shown in Fig. 3 (g,h,i). Although the spatial resolution mismatches between GRACE (Fig. 3 d,e,f) and PCR-GLOBWB (Fig. 3 g,h,i) were presented, the signal location between them was relatively consistent. To verify the consistency of the location,

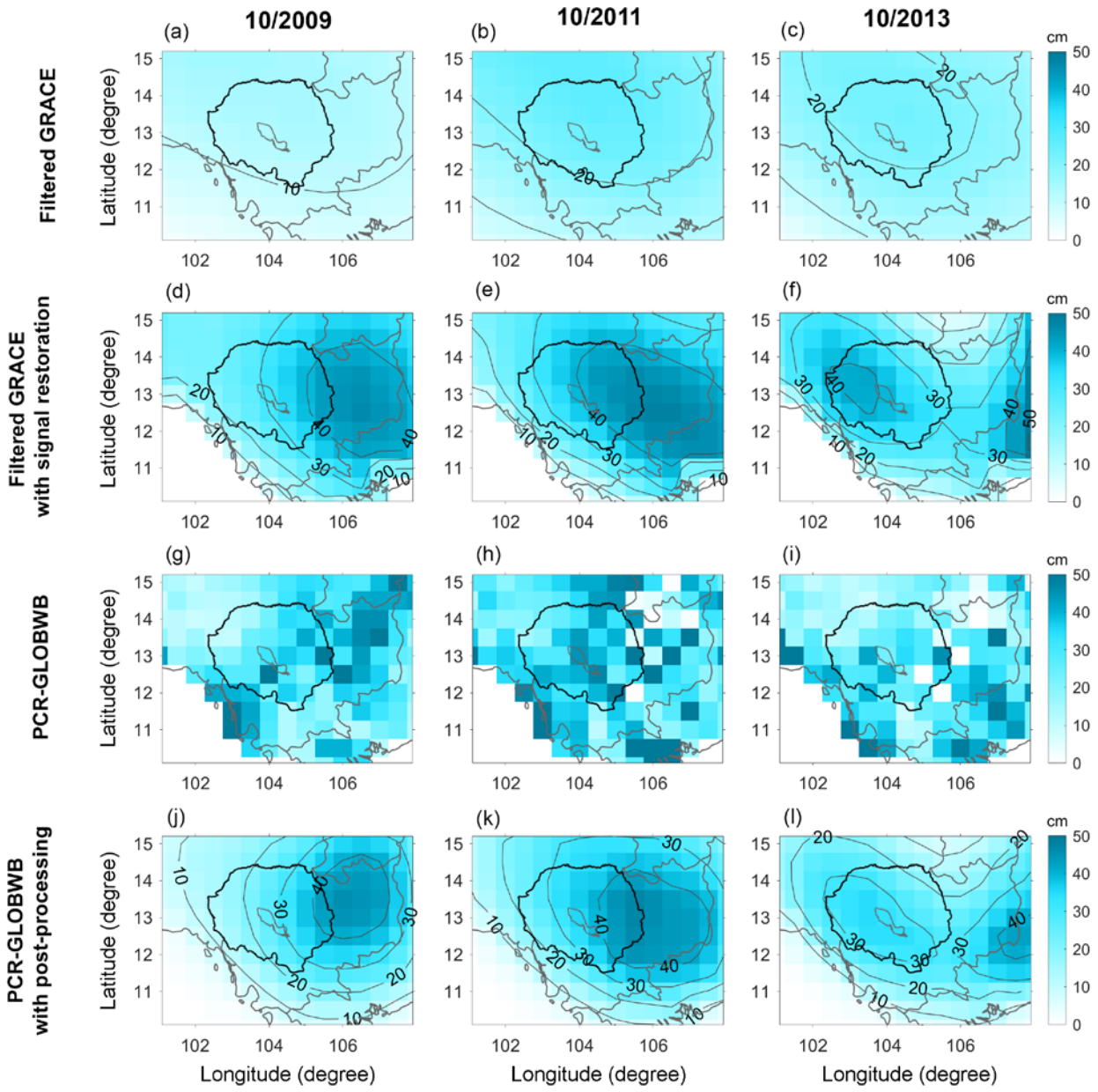

289

290 **Fig. 3:** TWS variation over Tonlé Sap basin in October 2009, 2011, and 2013 derived from GRACE
291 solution before (a,b,c) and after signal restoration applied (d,e,f). PCR-GLOBWB results of the same
292 months are also shown (g,h,i). For the comparison with GRACE, the same post-processing procedures
293 used for GRACE were applied to PCR-GLOBWB (see Sect. 3.1 and 4), and results were shown in the last
294 row (j,k,l).

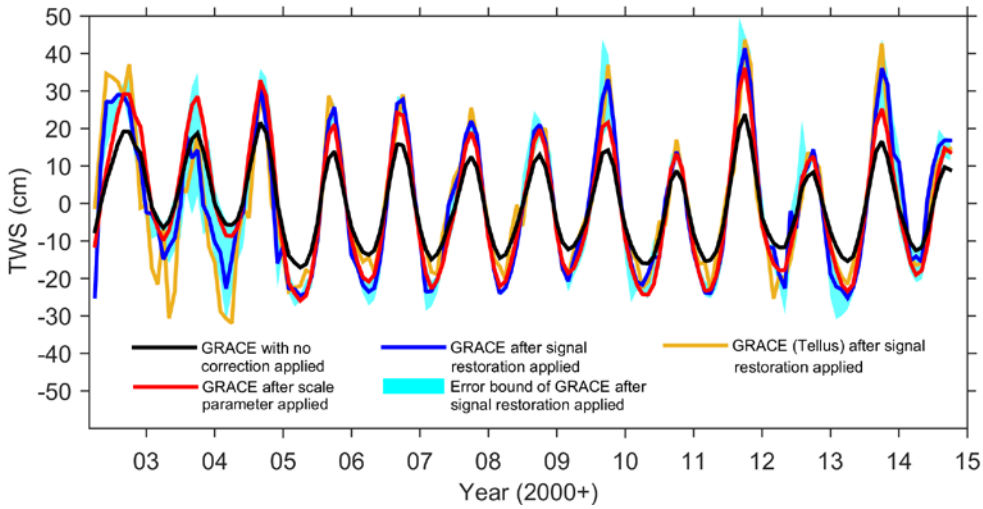

Fig. 4: TWS averaged over Tonlé Sap basin derived from different GRACE solutions and correction methods.

the same GRACE post-processing procedures (see Sect. 3.1 and 4) were applied to PCR-GLOBWB, and the results were shown in Fig. 3 (j,k,l). Again, although not identical, the spatial distribution was observed very close to GRACE signal restoration results. Note that the PCR-GLOBWB with post-processing was only used to illustrate the consistency of the TWS spatial distribution and was not used further in this study.

Fig. 4 presents the basin averaged TWS variations based on different GRACE solutions and correction methods. The filtered TWS without any correction applied is very smooth with a clear seasonal signal varying within the range of approximately ±10 cm EWH. After applying the signal restoration method to the GRACE solutions, the amplitude of the TWS variations increases by approximately a factor of two. Note that the amplitude of the corrected TWS was always approximately 20 cm EWH, even though different *R* values were used (see Table 1). This indicates that, for the average signal amplitude estimated over a long time interval, the signal restoration is sufficiently insensitive to the choice of *R*. In some specific months, however, a difference is observed. This is likely due to the remaining error caused by the choice of an *R* value that was too small (i.e., stripes may still exist in that case).

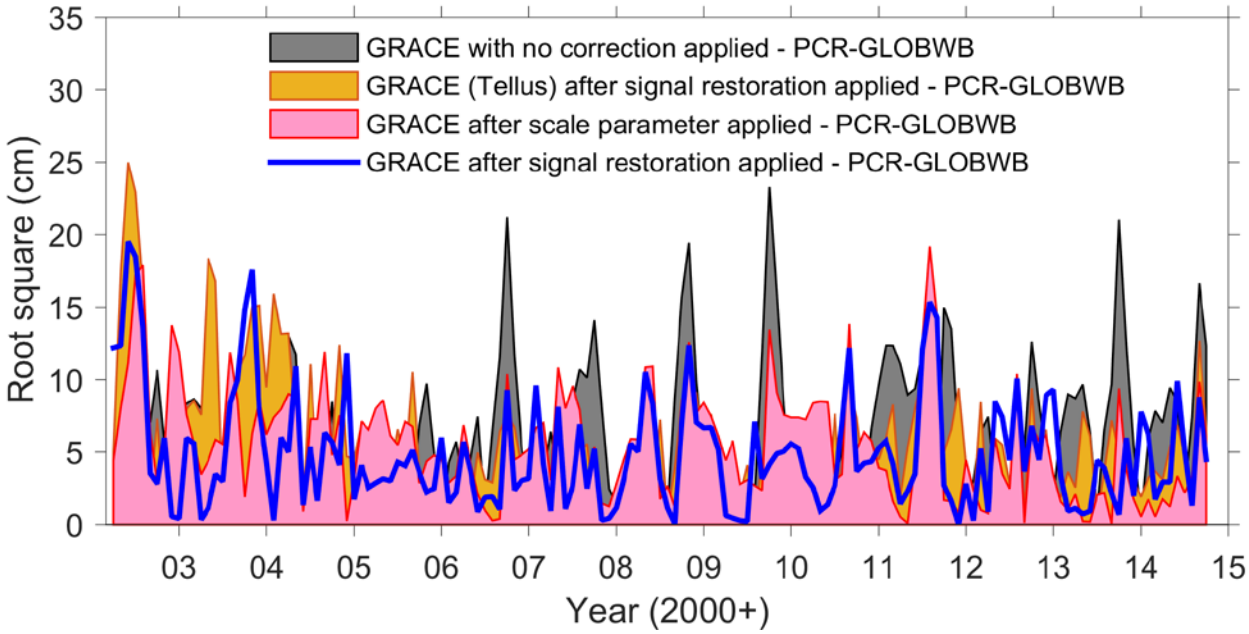

312

313 **Fig. 5:** Absolute value of the root-square difference between TWS based on various GRACE solutions
314 and TWS from PCR-GLOBWB ($\sqrt{(\text{GRACE} - \text{PCRGLOBWB})^2}$). A value closer to zero indicates a closer match to
315 the PCR-GLOBWB.

316 For the comparison, the corrected TWS was also computed from the GRACE solutions using the scale
317 parameter method. Note that, in contrast to the signal restoration method, which computes a correction for
318 each month individually, the scale parameter method uses the same scale parameter for all months. In this
319 way, the annual amplitude increased to approximately 20 cm EWH. Although the resulting time series
320 after the two correction methods show a similar pattern (see Fig. 4), the overall amplitude after the scale
321 parameter method is smaller, particularly during the flood events, e.g., in October 2011 and October 2013.
322 On the other hand, large differences can also be seen in October 2003, where the scale parameter method
323 led to significantly larger TWS variation. To assess which technique might better characterize the true
324 TWS in the region, the next section compares the results to the output from the hydrological models.

325

Table 1: Correlation coefficient and RMS difference between GRACE-based TWS and TWS from PCR-GLOBWB. Annual amplitude and phase (estimated using Eqs. B1–B3) of TWS variations from various GRACE solutions and hydrological models are also provided. The best performing correction method is highlighted in bold.

	Correlation wrt PCR-GLOBWB	RMS difference wrt PCR-GLOBWB (cm)	Annual amplitude (cm EWH)	Annual phase (month)
No correction GRACE (350 km)	0.91	7.84	13.6 ± 0.4	5.70 ± 0.05
Scale parameter GRACE (350 km)	0.91	7.60	20.7 ± 0.7	5.70 ± 0.05
Signal restoration GRACE (300 km)	0.85	8.90	22.4 ± 1.4	5.51 ± 0.10
Signal restoration GRACE (350 km)	**0.92**	**7.43**	**21.6 ± 1.0**	**5.77 ± 0.06**
Signal restoration GRACE (400 km)	0.90	7.64	20.7 ± 0.9	5.56 ± 0.07
Signal restoration GRACE (450 km)	0.90	7.48	20.2 ± 0.8	5.67 ± 0.07
Signal restoration GRACE (500 km)	0.89	8.13	20.9 ± 0.8	5.55 ± 0.08
Signal restoration GRACE (Tellus)	0.91	7.54	20.7 ± 0.9	5.52 ± 0.09
PCR-GLOBWB	-	-	21.5 ± 0.7	5.81 ± 0.06
PCR-GLOBWB (SM)	-	-	8.3 ± 0.2	4.90 ± 0.05
GLDAS-NOAH	-	-	14.6 ± 0.4	4.84 ± 0.08
ERA-Interim	-	-	7.5 ± 0.3	4.48 ± 0.08

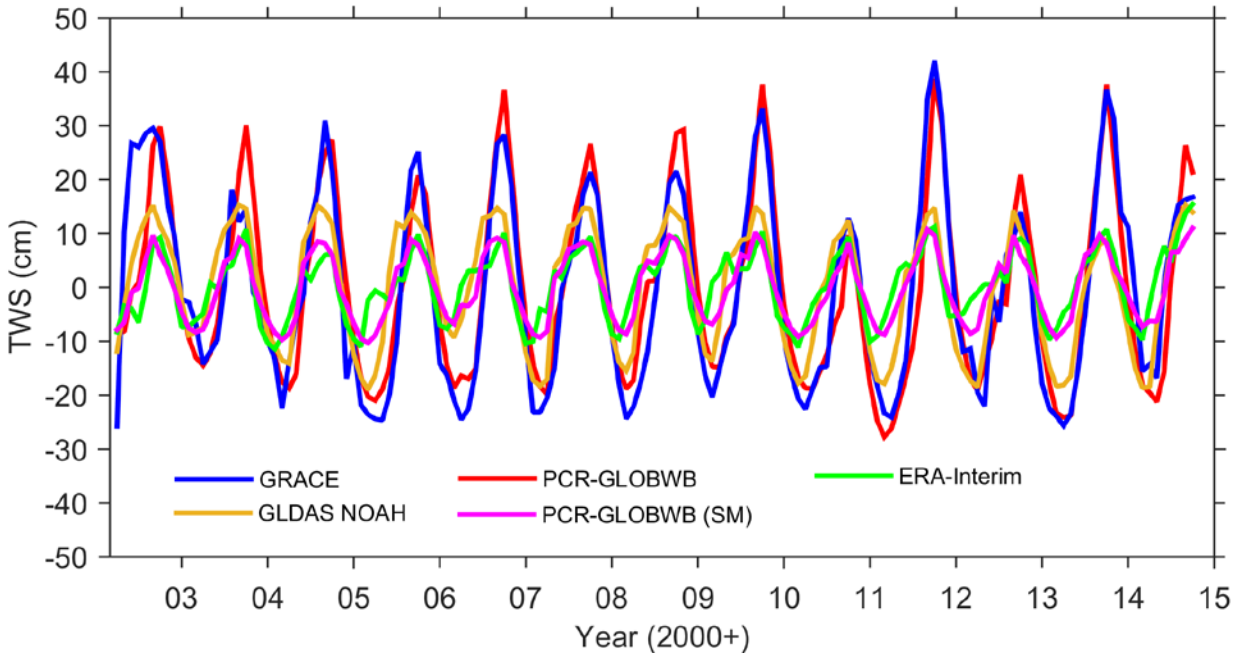

Fig. 6: TWS averaged over Tonlé Sap basin derived from GRACE solutions (with signal restoration applied), and hydrological models. PCR-GLOBWB includes soil moisture, groundwater, and surface water components. GLDAS-NOAH includes soil moisture and canopy water storage components. Only soil moisture component is covered by ERA-Interim and PCR-GLOBWB (SM).

5.1.2 GRACE versus PCR-GLOBWB

Because the TWS derived from the PCR-GLOBWB model covers all storage components, that model was used in the first instance as an additional comparison to the GRACE results. Fig. 5 shows differences between TWS based on various GRACE solutions and TWS from PCR-GLOBWB. The amplitude and phase were also estimated, based on Eqs. (B1–B3). Although not uniformly, the GRACE solutions after signal restoration (with R=350 km) show a closer match to PCR-GLOBWB, particularly after 2005, than the other solutions. Even though PCR-GLOBWB was used in the scale parameter estimation (see Sect. 4), the GRACE-based result after the scale parameter applied was not closer to the PCR-GLOBWB result than the result from the signal restoration method. Applying a uniform scale parameter to the entire time-series likely led to the insufficient flexibility of that correction.

Additionally, the statistical values given in Table 1 demonstrate that applying signal restoration with different *R* led to similar results. The GRACE-based TWS after the signal restoration with *R*=350 km was selected for further analysis, as it matches best to PCR-GLOBWB in terms of correlation coefficient and RMS difference.

5.1.3 Comparison of hydrological models

The basin averaged TWS variations derived from GRACE solutions and three hydrological models are shown in Fig. 6. As TWS variations derived from GLDAS and ECMWF lack surface water and groundwater contributions (so that the primary signal there is related to soil moisture (SM)), PCR-GLOBWB derived SM alone is also shown for a comparison (defined as PCR-GLOBWB (SM)). From Fig. 6 and Table 1, one can see that PCR-GLOBWB matches GRACE better than the other models, in terms of amplitude, phase and RMS difference. Such a good agreement justifies the primary usage of PCR-GLOBWB for the cross-comparison of GRACE-based estimates presented in the previous section.

Furthermore, the similar performance of GLDAS, ERA-Interim, and PCR-GLOBWB (SM) models is noteworthy, and suggests that the SM component is well characterized by all three models. To assess the role of the individual storages in TWS variations, the contribution percentage of the store ($w_{\%}$)) can be simply computed as follows:

$$w_{\%} = \left[\frac{1}{T}\sum_{t=1}^{T}\frac{w_t}{TWS_t}\right] \times 100 \qquad (2)$$

where w_t and TWS_t are the hydrological components and TWS variations estimated at time t and T is the total time interval of the time series considered. A comparison of PCR-GLOBWB (SM) with PCR-GLOBWB shows that SM contributes with only 24.5% to the TWS variation averaged over the entire Tonlé Sap basin (see Fig. 6), while the groundwater storage (GWS) is the major contributor (71.1 %). The remaining contribution is mostly provided by surface water (including reservoir, lake, irrigation paddy storages, and river channel storages): approximately 4.4%. Interception storage variation contributes less

than 0.001%. Note that the percentage values were computed based on the entire time series. A phase lag of approximately one month is observed between TWS and SM. This phase difference is explained mainly by the GWS component: it takes water several weeks to transfer from upper to lower layers (e.g., from surface to GWS).

Considering only the positive peak of every year, the lowest peak in the GRACE-derived TWS variations is detected in October 2010: 12.6 cm EWH. This peak is 49 % lower than the mean peak value (computed from all the peaks between 2002 and 2014). The second lowest peak is observed in October 2012: 44 % lower than the mean peak value. These features are also seen in the PCR-GLOBWB results. Additionally, the greatest flood event was seen as the highest TWS peak observed in October 2011 (by both GRACE and PCR-GLOBWB), quantified as approximately 42 cm EWH, which is 40% higher than the mean peak value. The second and the third largest flood events are observed in October 2013 as approximately 36 cm EWH (~34% higher than the mean peak) and October 2009 as approximately 33 cm EWH (~31% higher), respectively. The TWS variations constructed using only the SM component show much lower variations in the peak value, approximately 10 cm EWH. The reason is that the SM storage is limited by a specific field capacity with a particular maximum value, and therefore the similar peak value (corresponding to the field capacity) is observed in both normal and flood years. This suggests that the inter-annual TWS variability in the Tonlé Sap basin is driven by the GWS component and explains the relatively low peak values of GLDAS and ERA-Interim models in that area.

5.2 Precipitation

Monthly total precipitation averaged over the Tonlé Sap basin was computed (Fig. 7) for a comparison with the estimated TWS variations. In addition, the seasonal precipitation was computed by accumulating the monthly data over 2 periods per year, May – October (monsoon season) and November – April (dry season). The pattern of annual precipitation variations slightly changed after 2009 and, as seen in 2010, 2012 and 2014, a shortage of precipitation during the monsoon period was responsible for the low TWS

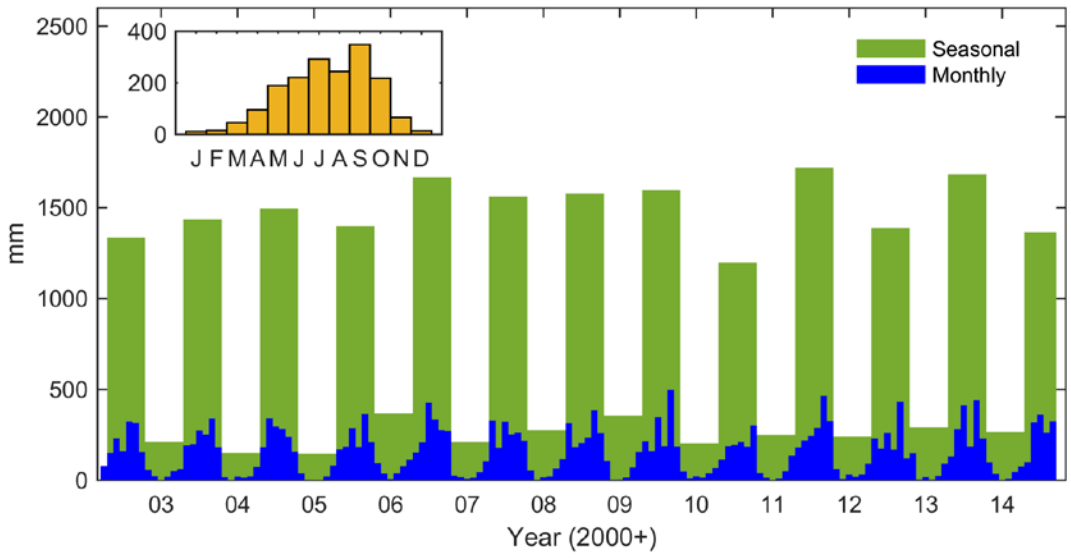

392

393 **Fig. 7.** Monthly and seasonal total precipitation over the Tonlé Sap basin derived from TRMM 3B43.
394 Seasonal precipitation was computed by accumulating the monthly data in 2 periods per year, May –
395 October and November – April. The mean value of a specific month is shown in the inset figure.

396 signatures seen in the GRACE TWS estimates. The largest amount of precipitation was recorded in 2011,
397 when precipitation in all the months of the monsoon period was higher than the average. This was likely
398 the reason for the greatest TWS observed in 2011 (see Fig. 6).

399 **5.3 Inundated area variations**

400 To observe variations of the inundated area, the monthly averaged NDWI values calculated from
401 MYD09A1 data were analyzed (Fig. 8). Large flood extents are seen in October 2011 and October 2013.
402 A limited inundated area is observed in October 2003, October 2012, and particularly in October 2010,
403 where the average NDWI falls below 0.3. To estimate the inundated area, the positive NDWI pixels inside
404 the maximum flood extent area (defined as a gray shaded area in Fig. 8 (n)) were counted. The maximum
405 flood extent polygon (outermost blue boundary line) was drawn based on the fact that the NDWI outside
406 the polygon (between July 2002 and October 2014) always has zero or negative values. Based on the
407 resolution of the surface reflectance data, each positive NDWI pixel was counted as 0.25 km^2.

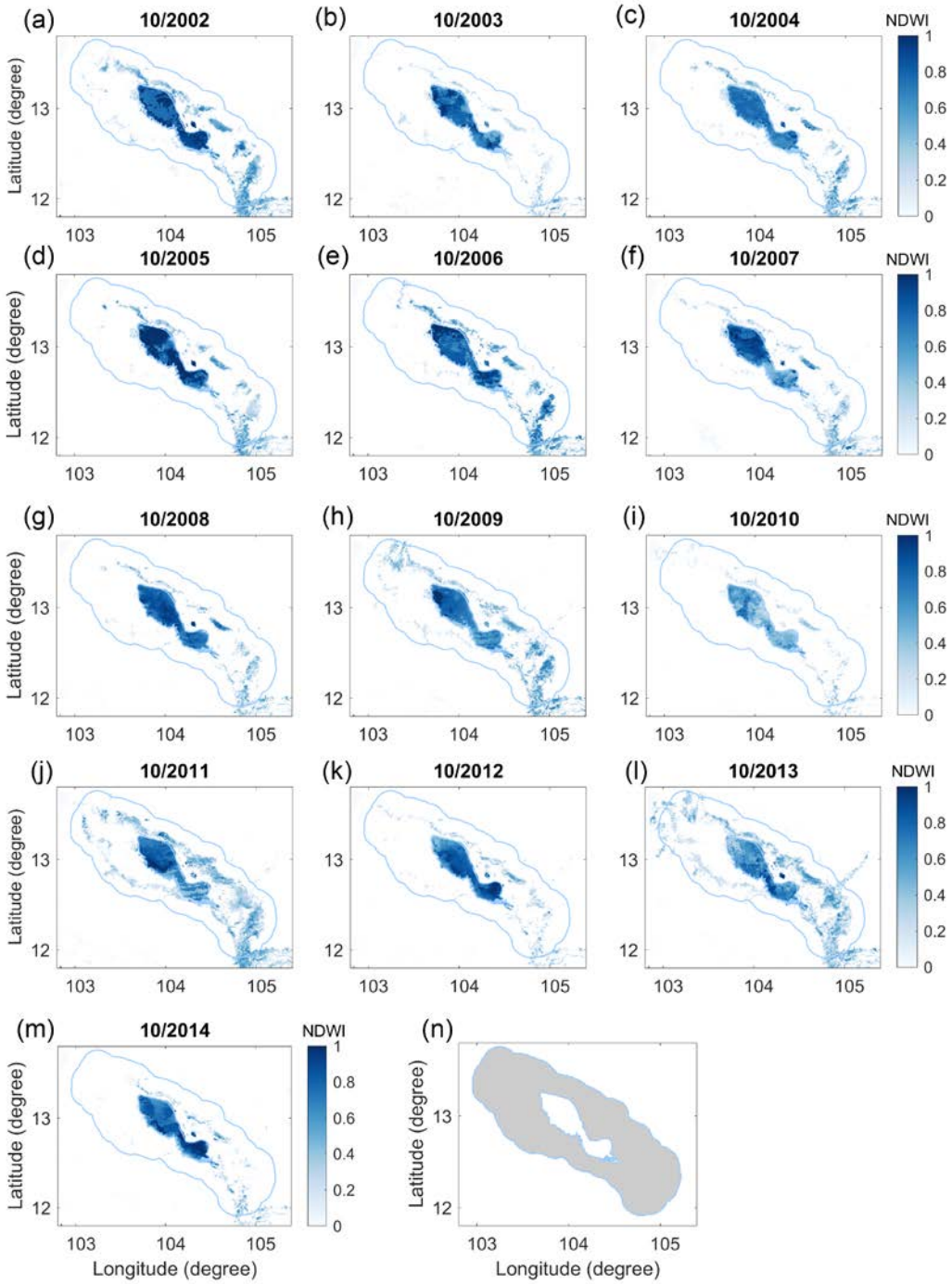

408

409 **Fig. 8.** Monthly mean NDWI [-] of October between 2002 and 2014. Zero and negative values are

410 excluded. The maximum flood extent is defined by the blue polygon. For the inundated area calculation,

411 only the NDWI values inside the gray shade area (see (n)) are used.

In contrast to the small proportion computed over the entire basin, the surface water estimated from PCR-GLOBWB contributes approximately 61.3% to the TWS variation averaged inside the Tonlé Sap floodplain. GWS is the second contributor (35.3%) while SM contributes only 3.4%. As the surface water is the major contributor, it is reasonable to represent the TWS variations in terms of inundated area variations. Therefore, the average TWS variation inside the Tonlé Sap floodplain (the shaded polygon in Fig. 8 (n)) was computed from GRACE data to investigate whether it has the same temporal pattern as MODIS-derived inundated area variations. The number of TWS pixels was 7 inside the floodplain, compared to 28 over the entire basin.

The inundated area variations and TWS variations over the Tonlé Sap floodplain correspond well to each other, with a correlation coefficient of 0.81 (Fig. 9). Note that the area within the maximum flood extent area (see Fig. 8 (n)) is only 21,300 km2 (equal to a linear resolution of ~146 km), which is 3.8 times smaller than the total area of the Tonlé Sap basin. Due to a limited GRACE spatial resolution, the GRACE-based estimates of TWS inside the floodplain area is close to the TWS estimates over the basin (see also Fig. 6). Therefore, even though the GRACE TWS inside the floodplain area was used in this section for the sake of consistency with the inundated area, the GRACE TWS estimate is rather a basin average signal and not a signal inside the floodplain only. On the other hand, a high correlation between GRACE TWS estimates and MODIS inundation area estimates implies a strong spatial correlation of mass re-distribution processes in the area, let the TWS inside the floodplain area and over the basin be driven by different hydrological processes, as described by PCR-GLOBWB.

From Fig. 9, the phase difference between the two time series is only 0.13 months, or approximately 4 days. The phase shift is likely due to the different data interval used to calculate the monthly average of the TWS and the inundated area variations. The mean peak inundated area, calculated by averaging all yearly peak values between September 2002 and September 2014, is 3,436 km^2. The lowest peak inundated area and lowest average TWS peak are observed in October 2010. The inundated area in that month was 1,342 km^2, i.e., 2.6 times less than the mean value. The largest inundated areas of 6,561 km^2

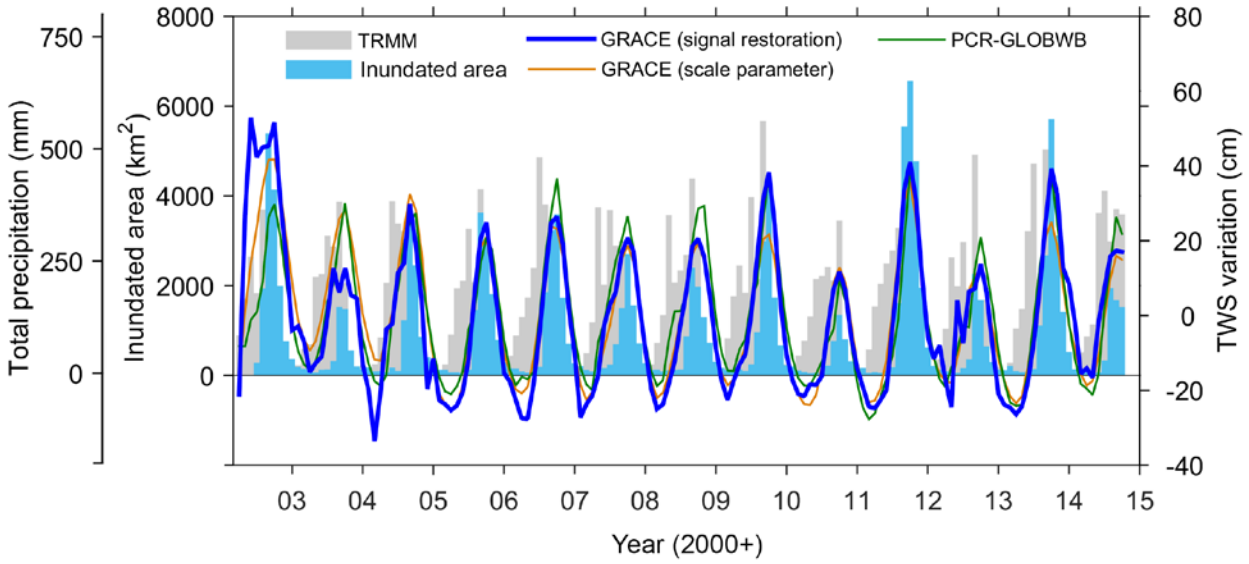

437

438 **Fig. 9:** Monthly inundated area and TWS variations (derived from GRACE solutions after signal
439 restoration applied, GRACE solutions after scale parameter method applied, and PCR-GLOBWB)
440 averaged inside the defined polygon (see Fig. 8 (n)). Total monthly precipitation (TRMM) is also provided.
441 Note that the zero positions are different in the left and right vertical axes.

442 (91% above the mean peak value) and 5,710 km^2 (66% above) are seen in October 2011 and 2013,
443 respectively. The similarity of the inundated area variations and the GRACE-derived TWS variations is
444 also seen in the late 2003 monsoon period. Interestingly, in line with the small inundated area in late 2003,
445 GRACE also observed the low TWS at the same period. This is in agreement with Kummu et al. (2014),
446 who showed that in 2003 the Tonlé Sap Lake received the smallest amount of rainfall (69.1 km^3/year;
447 measured at Cambodian weather stations) since 1999. Remarkably, the aforementioned feature is not
448 present in PCR-GLOBWB, GRACE data with the scale parameter correction, and the global precipitation
449 data (see Fig. 9). According to Kummu et al. (2014), it is likely that the precipitation in the global dataset
450 is overestimated during the late 2003 monsoon period. As PCR-GLOBWB was forced by this dataset,
451 PCR-GLOBWB likely overestimated TWS in

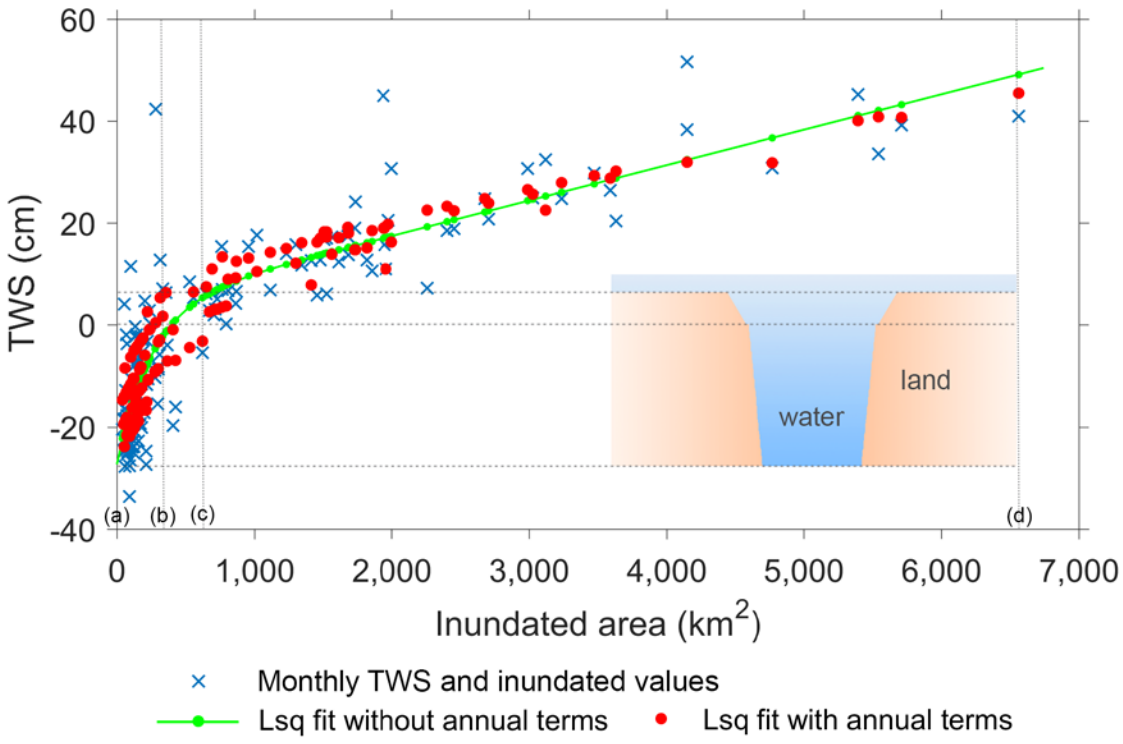

452

453 **Fig. 10.** Scatter plot between TWS variation and inundated area before (original, blue crosses), and after
454 applying a least-squares fit with (red dots) and without (green line) an annual variation term. Insert image
455 explains schematically the relationship between the TWS and inundated area with respect to the
456 topography of the inundation area.

457 this period. As far as the scale-corrected GRACE data are concerned, it is likely that the artifact in 2003 is
458 caused by applying a uniform scale parameter to the entire time-series.

459 Next, a quantitative relationship between the inundated area and the TWS variation is investigated. The
460 scatter plot of these two quantities shows a non-linear behavior (Fig. 10). A different slope is seen
461 between, e.g., points (a) to (b) and points (c) to (d), which is presumably due to the topography of the
462 inundation area. Water is firstly accumulated inside the deeper inundation bank (e.g., between points (a)
463 and (c)), and therefore a large rise in TWS is not accompanied by a significant increase in inundated area.
464 During the wet season, when the deeper inundation bank is filled, water forms a shallow layer over a large
465 inundation area, and even a small change in TWS can lead to a large variation of the inundated area (e.g.,

between points (c) and (d)). From Fig. 10, a relationship between the inundated area and the TWS variation can be established, e.g., using a simple polynomial regression. It is found that the residual (between the fit and the target) was further reduced when the annual variation term was also used in the regression equation. The equation used to relate the inundated area to the TWS variation in this study was ultimately defined as

$$y = a_0 + a_1 x + a_2 \exp(b) + \overbrace{a_3 cos(\omega t) + a_4 sin(\omega t)}^{\text{annual variation}} \quad , \tag{2}$$

$$b = \frac{-x}{1000\ \text{km}^2} \tag{3}$$

where y is a vector containing the TWS variations (m) derived from GRACE, and x is a vector containing the inundated area (km^2) estimates derived from NDWI. The fourth and fifth terms represent annual variations, where t is the observation time, and $\omega = 2\pi/T$ with T the annual period. Using least-squares adjustment, we estimated the coefficients in Eq. (2) and their values are given in Table 2. Fig. 11(a) and Table 3 show a good agreement between the TWS variations estimated on the basis of the MODIS-derived inundated area and the GRACE-based ones, with a correlation coefficient of 0.92 and a RMS difference of 7.65 cm EWH, when the annual variation term is included. The correlation coefficient reduces to 0.88 and the RMS difference increases by 14% when the annual variation term is not included.

The need of annual terms is explained by the presence of the stationary annual signal from the soil moisture component (see Fig. 6). This suggests that in order to ensure the consistency of results with the TWS signal properties, the annual variation should be included in the adjustment. To support our interpretation, the annual variation terms in Eq. (2) are replaced by the soil moisture signal from PCR-GLOBWB:

$$y = a_0 + a_1 x + a_2 \exp(b) + a_5 SM \tag{4}$$

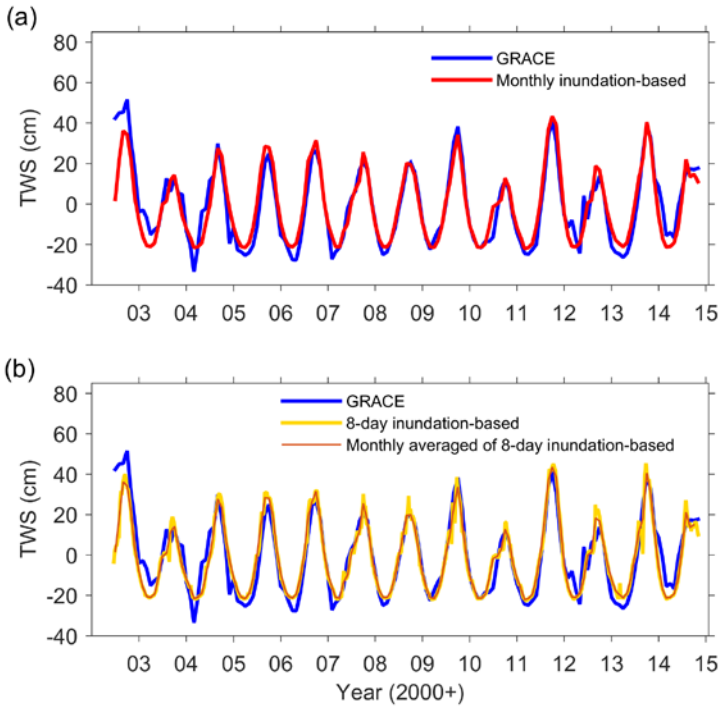

Fig. 11. TWS averaged over the maximum flood extent area (see Fig. 9 (n)) derived from the mean monthly MODIS-derived inundated area (a), and from the 8-day mean MODIS-derived inundated area (b). In (b), the monthly averaged was computed from the 8-day result. GRACE-based TWS estimates are shown in both plots for a reference. The annual variation terms are included based on Eq. (2).

Table 2: Parameters estimated from least-squares adjustment using Eq. (2) – (4) with and without including annual variation terms.

	Without annual variation terms	With annual variation terms	With annual variation terms from SM
a_0 (m)	3.6 ± 0.7	$-5.4\times10^{-1} \pm 6.4\times10^{-1}$	1.2± 0.7
a_1 (m/km^2)	$1.7\times10^{-3} \pm 1.2\times10^{-4}$	$1.4\times10^{-3} \pm 1\times10^{-4}$	$1.4\times10^{-3} \pm 1\times10^{-4}$
a_2 (m)	-30.6 ± 1.6	-16.2 ± 1.4	-20.6 ± 1.4
a_3 (m)	0	-4.8 ± 0.9	0
a_4 (m)	0	-9.2 ± 0.9	0
a_5 (-)	0	0	0.9 ± 0.1

Table 3: Correlation coefficient and RMS difference between the MODIS-derived inundation-based TWS variations and the GRACE-based ones. In the former case, the estimation process made use of the mean monthly inundated area and the mean 8-day inundation area.

Monthly MODIS-derived inundation-based	Correlation coefficient	RMS difference (cm EWH)
No annual variation term	0.884	8.94
With annual variation term	0.921	7.65
With annual variation term from SM	0.908	7.98
8-Day MODIS-derived inundation-based		
No annual variation term	0.884	8.95
With annual variation term	0.920	7.70
With annual variation term from SM	0.911	7.87

where SM is the soil moisture component (m). The coefficients estimated from Eq. (4) are also given in Table 2. Again, good agreement between the GRACE-based and MODIS-based values is observed with a similar correlation and RMSE values as obtained based on Eq. (2) (see Table 3). Importantly, the restoration of the annual variation (either from the mathematical fit or from SM component) is necessary to increase the accuracy of the adjustment.

The analysis above was based on the monthly data. Further investigation was conducted to determine whether the same relationship could be applied with a higher temporal sampling. The 8-day MODIS-derived inundated areas were firstly converted to TWS variations (using Eq. (2) with the same coefficients) and then averaged over monthly intervals (Fig. 11(b)). The TWS variations estimated this way are again compared to GRACE-based TWS variations (Fig. 11(b) and Table 3). For completeness, the adjustment based on Eq. (4) was also performed. The obtained correlations and RMS differences are very similar to those based on the mean monthly inundated areas. Such a good agreement is an indication that reflectance data can be employed to observe the sub-monthly (e.g., 8-day) TWS variations over the Tonlé Sap basin, and potentially at spatial scales higher than that GRACE data can reliably provide.

5.4 Inter-annual variations

To explore annual and inter-annual variations of hydrological activity over the Tonlé Sap basin, power spectra were computed based on the Morlet wavelet with the software provided by Torrence and Compo (1998). The wavelets are used to estimate the dominant time-frequencies (periods) for different time-series. We analyzed the monthly averaged TWS estimates derived from GRACE and PCR-GLOBWB (Fig. 12 (a), (b)), the monthly averaged SM, GWS, and surface water storage derived from PCR-GLOBWB (Fig. 12 (c), (d), (e)), the monthly inundated area (over the defined flood extent; Fig. 12 (f)), as well as the monthly averaged global precipitation (Fig. 12 (g)). As the precipitation is a derivative of water storage, we integrated precipitation over time before computing its power spectrum to avoid mathematical artifacts caused by the spectral inconsistency. In all spectra, annual variations are clearly observed throughout the entire study interval. Starting from October 2010, inter-annual variations with an approximately 2-year period are present in all spectra, except PCR-GLOBWB (SM), for which the limitation of the SM storage capacity is likely the cause. The SM storage cannot exceed a certain amount and therefore only a regular seasonal variation was observed from the SM spectrum. From Fig. 12 (d), it is clear that GWS has the strongest 2-year cycle of the three considered PCR-GLOBWB components. In fact, the shown power spectra of inter-annual variations reflect their relative amplitudes (compared to the total signal). The amplitudes of GWS inter-annual variations seem to be larger simply because that signal is cleaned from nearly all stationary soil moisture signal. Inter-annual variations of open water can also be observed from the surface water storage (PCR-GLOBWB (Surface), Fig. 12 (e)) and the MODIS-derived inundated area (Fig. 12 (f)). It is noted that although the power spectrum of surface water storage was computed over the entire basin, the spectral pattern is identical when it was computed over the flood extent only (not shown). This is explained by the fact that the surface water component was only situated inside the floodplain area. Therefore, the comparison between the spectra of PCR-GLOBWB (Surface) and the MODIS-derived inundated area based on Fig. 12 is reasonable. Due to the coarse spatial resolution of the remote sensing

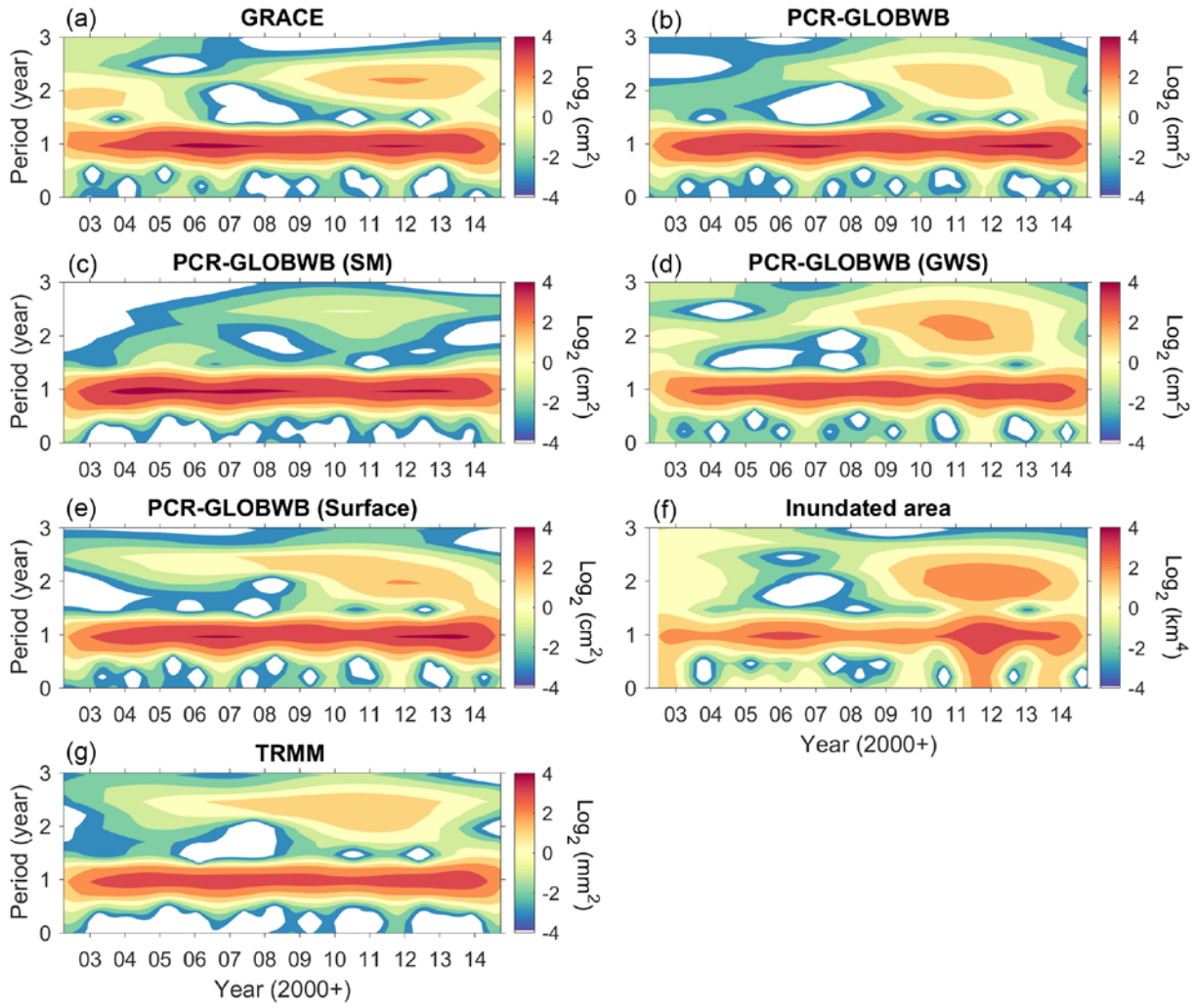

537

538 **Fig. 12.** Power spectral distribution of (a) GRACE-derived TWS, (b) PCR-GLOBWB derived TWS, (c)
539 PCR-GLOBWB derived soil moisture, (d) PCR-GLOBWB derived groundwater storage, (e) PCR-
540 GLOBWB derived surface water storage, (f) MODIS-derived inundated area, and (g) TRMM monthly
541 precipitation (integrated over study period). The power spectra are presented in the base-2 logarithmic
542 scale.

543 observations, similar spectra patterns of TWS, SM, GWS, and TRMM as Fig. 12 were also observed even
544 when only the signal inside the floodplain was considered (not shown). The inter-annual amplitude of the
545 MODIS-derived inundated area (Fig. 12 (f)) is stronger than that of surface water storage (Fig. 12 (e)) and
546 even of TWS (Fig. 12 (a), (b)). This can be explained by the non-linear relationship described earlier

between the inundated area and the TWS: small variations of TWS can cause large variations in the inundated area during the flood period (see the discussion in Sect. 5.3). The 2011 and 2013 floods apparently led to stronger inter-annual amplitude of the inundated area variations than of TWS variations. Finally, it is not surprising that the TWS power spectra resemble that of precipitation (Fig. 12 (g)), since the latter is the source of the observed TWS variations.

6. Discussion and conclusions

Satellite remote sensing data of several types as well as several hydrological models were used to study the TWS variations and flood signatures over the Tonlé Sap basin between 2002 and 2014.

Among the satellite observations, the major focus was on GRACE, which observes the TWS variations directly. Applying the signal restoration method to GRACE data improves the accuracy of the TWS estimates. In contrast to the scale parameter method that applies the same scale parameter to all monthly data, the signal restoration method treats TWS differently for different months. This improves the ability of GRACE-based estimates to capture the irregularly low and high (e.g., flood) TWS signatures. Of course, it is worth keeping in mind that only the signal over one particular basin was analyzed in this study, and the performance of the signal restoration method may be different in other regions. Furthermore, the optimal choice of implementation details (for example, Gaussian smoothing radius and stopping criterion) may be different in other areas. Ideally, the choice of the stopping criterion should be such that additional iterations do not significantly affect the final result, so that the total number of iterations can be very large. However, in practice, each iteration introduces an additional error, e.g., due to the Gibbs phenomenon (Swenson and Wahr, 2002) or the presence of North-South stripes in the filtered reference TWS. Therefore, the iterations should be stopped before the errors become too large. Further sensitivity studies on the impact of implementation details are recommended to facilitate the use of the signal restoration method in various regions.

571 Using observations from more than one independent source was necessary to interpret and validate the
572 GRACE-based TWS estimations. Due to the absence of several important components (in particular,
573 groundwater) in some hydrological models, a mismatch in amplitude and phase was observed compared to
574 GRACE. The PCR-GLOBWB hydrological model, on the other hand, covers all the major contributors to
575 TWS (including groundwater and surface water), allowing the results to be directly compared to GRACE.
576 Furthermore, usage of the PCR-GLOBWB model allows the contributions of the different storage
577 components to be quantified, yielding an improved understanding of their dynamics. Irregular
578 precipitation variations between 2010 and 2014 observed from TRMM verify the low and high TWS
579 variation in the same period.

580 The inter-annual TWS variations between 2010 and 2014 were driven by the variability of the
581 precipitation seasonal amplitude that began from 2009. The inter-annual variations were mainly present in
582 the GWS and surface water storage components. The SM component lacks those variations due to its
583 limited storage capacity. Although the 2010-2014 inter-annual patterns were clearly visible, it is difficult
584 to verify their long-term continuity due to the limited understanding of the driving mechanisms. Longer
585 time series are needed for better understanding of the phenomenon.

586 It was shown that the inundated area variations derived from surface reflectance observations can also
587 provide valuable information for GRACE data validation. It was shown for the first time that the
588 reflectance data can be successfully used to estimate the total TWS variations. To that end, an empirical
589 non-linear relationship between the inundated area and GRACE-based TWS variations was established for
590 the Tonlé Sap basin. The non-linear relationship constructed can also be used to explain the topography of
591 the inundation area. The relationship reveals that only small change of the TWS can lead to a significant
592 variation of the inundated area in the wet season. It is also found that including the annual signal is
593 necessary in the adjustment process in order to reduce the RMS values. The source of the annual variation
594 is the soil moisture component, which does not correlate with the inundation area variation signal. Further
595 analysis showed a good agreement between the 8-day MODIS-derived TWS variations averaged over

monthly intervals and the GRACE TWS variations. This indicates that surface reflectance data can also be used to estimate TWS at sub-monthly time scales, provided that monthly GRACE-based TWS variations are used as a "training" phase. It is likely that the approach developed would have similar applications to other areas that experience regular large-scale inundation where NDWI has strong correlation with TWS. More case studies conducted over other regions are needed to confirm the performance of the approach.

Although this study made use of the state-of-the-art satellite data, higher accuracy of the data is still welcome in order to achieve more accurate descriptions of flood events. This might be possible if data from new satellite missions are used that are already operational or will become operational in the near future. For example, the Sentinel-2 mission (Drusch et al., 2012) will provide surface reflectance data with a temporal resolution of 5 days and a spatial resolution of 60 m or higher (Sentinel-2A was launched in June 2015; Sentinel-2B is to be launched in the middle of 2016). The Global Precipitation Measurement mission (GPM; Hou et al., 2014) has provided global near real-time rainfall data since March 2014 with a spatial resolution of approximately 10 km. GPM data can be used to force the next version of PCR-GLOBWB model, which will provide global near real-time TWS estimates with a similar spatial resolution (Sutanudjaja et al., in prep.). Additionally, the variation of the Tonlé Sap Lake level could be measured to a very high accuracy using future altimetry satellite observations, e.g., Sentinel-3 (Donlon et al., 2012), ICESat-2 (Abdalati et al., 2010) and SWOT (Durand et al., 2010). Finally, the GRACE Follow-On mission (Flechtner et al. 2014; launch scheduled in August 2017) is expected to continue delivering monthly gravity field products well into the next decade. By utilizing these state-of-the-art satellite observations and hydrological models, the monitoring of flood events and their impact will continue to improve.

Acknowledgement

This research was funded by The Netherlands Organization for Scientific Research, NWO (project number 842.00.006). The research was also sponsored by the NWO Exacte Wetenschappen, EW (NWO Physical Sciences Division) for the use of supercomputer facilities, with financial support from NWO. Authors would like to thank Doug Alsdorf and two anonymous reviewers for their valuable suggestions that significantly improved the quality of the manuscript.

7. References

Abdalati, W., Zwally, H. J., Bindschadler, R., Csatho, B., Farrell, S. L., Fricker, H. A., et al. (2010). The ICESat-2 laser altimetry mission. Proceedings of the IEEE, 98, 735–751.

Arias, M. E., Cochrane, T. A., Piman, T., Kummu, M., Caruso, B. S., & Killeen, T. J. (2012). Quantifying changes in flooding and habitats in the Tonlé Sap Lake (Cambodia) caused by water infrastructure development and climate change in the Mekong Basin. *Journal of Environmental Management*, *112*, 53–66. doi:10.1016/j.jenvman.2012.07.003.

Bettadpur, S. (2012). Gravity recovery and climate experiment, UTCSR level-2 processing standards document for level-2 product release 005. GRACE 327-742 (CSR-GR-12-xx), Center for Space Research, The University of Texas at Austin, 17 pp.

Baur, O., Kuhn, M., & Featherstone, F. E. (2009). GRACE-derived ice-mass variations over Greenland by accounting for leakage effects. *Journal of Geophysical Research*, *114*, B06407. doi:10.1029/2008JB006239.

Cochrane, T. A., Arias, M. E., & Piman, T. (2014). Historical impact of water infrastructure on water levels of the Mekong River and the Tonlé Sap system. *Hydrology Earth System Sciences*, *18*, 4529–4541. doi:10.5194/hess-18-4529-2014.

641 Chen, J., Li, J., Zhang, Z., & Ni, S. (2014). Long-term groundwater variations in Northwest India from
642 satellite gravity measurements. *Global and Planetary Change*, *116*, 130–138.
643 doi:10.1016/j.gloplacha.2014.02.007.

644 Chen, J. L., Wilson, C.R., & Tapley, B.D. (2013). Contribution of ice sheet and mountain glacier melt to
645 recent sea level rise. *Nature Geoscience*, *6*, 549–552. http://dx.doi.org/10.1038/NGEO1829.

646 Cheng, M., &Tapley, B. (2004). Variations in the Earth's oblateness during the past 28 years, *Journal of*
647 *Geophysical Research*, *109*(*B09402*), doi:10.1029/2004JB003028.

648 Dahle, C., Flechtner, F., Gruber, C., König, D.,König, R., Michalak, G., & Neumayer, K.-H. (2014). GFZ
649 RL05: An Improved Time-Series of Monthly GRACE Gravity Field Solutions. In Flechtner, F.,
650 Sneeuw, N., Schuh, W.-D. (Eds.), Observation of the System Earth from Space - CHAMP,
651 GRACE, GOCE and future missions, (GEOTECHNOLOGIEN Science Report; 20; Advanced
652 Technologies in Earth Sciences), Berlin, Springer, 29-39, http://doi.org/10.1007/978-3-642-
653 32135-1_4.

654 Dee, D. P., Uppala, S. M., Simmons, A. J., Berrisford, P., Poli, P., Kobayashi, S., et al. (2011). The ERA-
655 Interim reanalysis: configuration and performance of the data assimilation system. *Quarterly*
656 *Journal of the Royal Meteorological Society*, *137*, 553–597, doi:10.1002/qj.828.

657 Donlon, C., Berruti, B., Buongiorno, A., Ferreira, M.-H., Féménias, P., Frerick, J., et al. (2012). The
658 Global Monitoring for Environment and Security (GMES) Sentinel-3 mission. *Remote Sensing of*
659 *Environment*, 120, 37–57. doi:10.1016/j.rse.2011.07.024.

660 Drusch, M., Del Bello, U., Carlier, S., Colin, O., Fernandez, V., Gascon, F., et al. (2012). Sentinel-2:
661 ESA's Optical High-Resolution Mission for GMES Operational Services. *Remote Sensing of*
662 *Environment*, *120*, 25–36.

663 Durand, M., Fu, L. L., Lettenmaier, D. P., Alsdorf, D. E., Rodrigues, E., and Esteban-Fernandez D. (2010).
664 The Surface Water and Ocean Topography mission: Observing terrestrial surface water and
665 oceanic sub-mesoscale eddies, Proceeding of the IEEE, 98(5), 766–779,
666 doi:10.1109/JPROC.2010.2043031.

667 Flechtner, F., Morton, P., Watkins, M., & Webb, F. (2014). Status of the GRACE follow-on mission, in
668 IAG symposium gravity, geoid, and height systems, 141,Venice, Italy, Springer, 117–121.

669 Hou, A. Y., Kakar, R. K., Neeck, S., Azarbarzin, A. A., Kummerow, C. D., Kojima, M., et al. (2014). The
670 global precipitation measurement mission. *Bulletin of the American Meteorological Society*, *95*,
671 701–722. doi:10.1175/BAMS-D-13-00164.1.

672 Huffman, G. J., Adler, R. F., Bolvin, D. T., Gu, G., Nelkin, E. J., Bowman, K. P., et al. (2007). The
673 TRMM multisatellite precipitation analysis (TMPA): Quasi-global, multiyear, combined-sensor
674 precipitation estimates at fine scales. *Journal of Hydrometeorology*, *8*, 38–55.
675 doi:10.1175/JHM560.1.

676 Jekeli, C. (1981). Alternative Methods to Smooth the Earth's Gravity Field. *Scientific Report*, *327*, School
677 of Earth Science, The Ohio State University.

678 Klees, R., Liu, X., Wittwe, T., Gunter, B. C., Revtova, E. A., Tenzer, R., et al. (2008). A Comparison of
679 Global and Regional GRACE Models for Land Hydrology. *Surveys In Geophysics*, *29*, 335–359.
680 doi:10.1007/s10712-008-9049-8.

681 Kummerow, C., Barnes, W., Kozu, T., Shiue, J., & Simpson, J. (1998). The Tropical Rainfall Measuring
682 Mission (TRMM) sensor package. *Journal of Atmospheric and Oceanic Technology*, *15*, 809–817.

683 Kummu, M., Tes, S.,Yin, S., Adamson, P., Józsa, J., Koponen, J., et al. (2014). Water balance analysis for
684 the Tonle Sap Lake–floodplain system. *Hydrological Processes*, *28*, 1722–1733.
685 doi:10.1002/hyp.9718.

686 Lamberts, D. (2001). Tonle Sap fisheries: a case study on floodplain gillnet fisheries in Siem Reap,
687 Cambodia. FAO Regional Office for Asia and the Pacific, Bangkok, Thailand. RAP Pub. 2001/11,
688 133 pp.

689 Landerer, F. W., & Swenson, S. C. (2012). Accuracy of scaled GRACE terrestrial water storage estimates.
690 *Water Resources Research*, *48*, W04531, doi:10.1029/2011WR011453.

691 Lim, P., Lek, S., Touch, S. T., Mao, S., & Chhouk, B. (1999). Diversity and spatial distribution of
692 freshwater fish in Great Lake and Tonle Sap river (Cambodia, Southeast Asia). *Aquatic Living*
693 *Resources*, *12*, 379−386.

694 Lu, J., Sun, G., McNulty, S. G., & Amatya, D. M. (2005). A comparison of six potential
695 evapotranspiration methods for regional use in the southeastern United States. *Journal of*
696 *American Water Resources Association, 41*, 621–633. doi:10.1111/j.1752-1688.2005.tb03759.x.

697 McFeeters, S. K. (1996). The use of the Normalized Difference Water Index (NDWI) in the delineation of
698 open water features. *International Journal of Remote Sensing*, *17*, 1425–1432. doi:
699 10.1080/01431169608948714, 1996.

700 NCDM, & UNDP (2014). Cambodia disaster loss and damage information system (CamDi), National
701 Commitee for Disaster Management and United Nations Development Programme. *Analysis*
702 *Report*, 1996-2013, Cambodia.
703 http://www.kh.undp.org/content/dam/cambodia/docs/EnvEnergy/Cambodia-Disaster-Loss-and-
704 Damage-Analysis-Report 1996- 2013.pdf (last access: 16 March 2015).

705 Peltier, W. R. (2004). Global glacial isostasy and the surface of the ice-age Earth: The ICE-5G 803 (VM2)
706 model and GRACE. *Annual Review of Earth and Planetary Sciences*, *32*, 111–149.

Reager, J. T., Thomas, B. F., & Famiglietti, J. S. (2014). River basin flood potential inferred using GRACE gravity observations at several months lead time. *Nature Geoscience*, *7*, 588–592. doi:10.1038/ngeo2203.

Rodell, M., Houser, P. R., Jambor, U., Gottschalck, J., Mitchell, K., Meng, C. J., et al. (2004). The global land data assimilation system. *Bulletin of the American Meteorological Society*, *85*, 381–394. doi: 10.1175/BAMS-85-3-381.

Rodell, M., Velicogna, I., & Famiglietti, J. S. (2009). Satellite-based estimates of groundwater depletion in India. *Nature*, *460*, 999–1002. doi:10.1038/nature08238.

Sakamoto, T., Nguyen, N. V., Kotera, A., Ohno, H., Ishitsuka, N., & Yokozawa, M. (2007). Detecting temporal changes in the extent of annual flooding within the Cambodia and the Vietnamese Mekong Delta from MODIS time-series imagery. *Remote Sensing of Environment*, *109*, 295–313. doi:10.1016/j.rse.2007.01.011.

Sutanudjaja, E. H., van Beek, L. P. H., de Jong, S. M., van Geer, F. C., & Bierkens, M. F. P. (2014). Calibrating a large-extent high-resolution coupled groundwater-land surface model using soil moisture and discharge data. *Water Resources Research*, *50*, 687–705. doi:10.1002/2013WR013807.

Sutanudjaja, E., van Beek, L. P. H., Drost, N., de Graaf, I., de Jong, K., Peßenteiner, S., et al. (in preparation). PCR-GLOBWB 2.0: a 5 arc-minute global hydrological and water resources model. *Geoscientific Model Development*.

Swenson, S., & Wahr, J. (2002). Methods for inferring regional surface-mass anomalies from Gravity Recovery and Climate Experiment (GRACE) measurements of time-variable gravity. *Journal of Geophysical Research, 107(B9)*, 2193. doi:10.1029/2001JB000576.

729 Swenson, S., Chambers, D., & Wahr, J. (2008). Estimating geocenter variations from a combination of
730 GRACE and ocean model output, *Journal of Geophysical Research*, *113*(*B08410*),
731 doi:10.1029/2007JB005338.

732 Tapley, B. D., Bettadpur, S., Ries, J. C., Thompson, P. F., & Watkins, M. M. (2004). GRACE
733 Measurements of Mass Variability in the Earth System. *Science*, *305*, 503–505,
734 doi:10.1126/science.1099192.

735 Thomas, A. C., Reager, J. T., Famiglietti, J. S., & Rodell, M. (2014). A GRACE-based water storage
736 deficit approach for hydrological drought characterization. *Geophysical Research Letters*, *41*,
737 1537–1545. doi:10.1002/2014GL059323.

738 Torrence, C., & Compo, G. P. (1998). A Practical Guide to Wavelet Analysis. *Bulletin of the American*
739 *Meteorological Society*, *79*, 61–78. doi: http://dx.doi.org/10.1175/1520-
740 0477(1998)079<0061:APGTWA>2.0.CO;2.

741 van Beek, L. P. H. (2008). Forcing PCR-GLOBWB with CRU data. Technical Report, Department of
742 Physical Geography, Utrecht University, Utrecht, The Netherlands.
743 http://vanbeek.geo.uu.nl/suppinfo/vanbeek2008.pdf.

744 van Beek, L. P. H. & Bierkens, M. F. P. (2009). The Global Hydrological Model PCR-GLOBWB:
745 Conceptualization, Parameterization and Verification. Technical Report, Department of Physical
746 Geography, Utrecht University, Utrecht, The Netherlands.
747 http://vanbeek.geo.uu.nl/suppinfo/vanbeekbierkens2009.pdf.

748 van Beek, L. P. H., Wada, Y., & Bierkens, M. F. P. (2011). Global monthly water stress: 1. Water balance
749 and water availability. *Water Resources Research*, *47*, W07517. doi:10.1029/2010WR009791.

Vermote, E. F., Kotchenova, S. Y., & Ray, J. P. (2011). MODIS surface reflectance user's guide version 1.3. Technical Report. http://modis-sr.ltdri.org/guide/MOD09_UserGuide_v1_3.pdf (last access: 30 May 2015).

Wada, Y., Wisser, D., & Bierkens, M. F. P. (2014). Global modeling of withdrawal, allocation and consumptive use of surface water and groundwater resources. *Earth System Dynamics, 5*, 15–40. doi:10.5194/esd-5-15-2014.

Wahr, J., Swenson, S., & Velicogna, I. (2006). Accuracy of GRACE mass estimates. *Geophysical Research Letters, 33*, L06401. doi:10.1029/2005GL025305.

Xiao, X., Boles, S., Frolking, S. Li, C., Babu, J. Y., Salas, W., & Moore III, B. (2005). Mapping paddy rice agriculture in South and Southeast Asia using multi-temporal MODIS images. *Remote Sensing of Environment, 100*, 95–113. doi:10.1016/j.rse.2005.10.004.

Yu, B., & Diao, X. (2011). Cambodia's agricultural strategy: Future development options for the rice sector, A policy discussion paper. *Special Report, 9*. International Food Policy Research Institute, Washington, D. C.

Appendix A: PCR-GLOBWB description

The state-of-the-art global hydrological model PCR-GLOBWB (van Beek, 2008; van Beek and Bierkens, 2009; van Beek et al., 2011; Sutanudjaja et al., 2011; Sutanudjaja et al., 2014; Sutanudjaja et al., in prep.) basically simulates spatial and temporal continuous fields of fluxes and storages in various water storage components (primarily, snow, soil moisture, surface water and groundwater) at a typical spatial resolution of 30 arc minutes (approximately 50 km at the equator). In brief, for each grid cell and for each daily time step, the model computes the storages of two vertically stacked soil layers and an underlying groundwater store based on water balance equation. Above the surface, the model also includes interception and snow

storages. For each cell, the model computes the vertical water exchanges between the soil layers and between the top layer and the atmosphere, i.e., rainfall and snowmelt, percolation and capillary rise, as well as evaporation and transpiration. The groundwater store underlies the soil and is fed by net groundwater recharge and exempt from direct influence of evaporation and transpiration fluxes. However, capillary rise from the groundwater store can occur depending on the simulated groundwater storage, surface elevation, and sustain soil moisture. Fluxes are simulated under various land cover types by considering sub-grid variations in topography, vegetation phenology, and soil properties. The model includes a physically-based scheme for infiltration and runoff, resulting in direct runoff, interflow, as well as groundwater baseflow and recharge. River discharge is calculated by accumulating and routing the specific runoff along the drainage network. In this study, the daily precipitation from the Tropical Rainfall Measuring Mission (TRMM) 3B42 V7 (Huffman et al., 2007), the daily mean 2 meter air temperature from ERA-Interim (Dee, 2011), and the daily reference potential evapotranspiration calculated based on Hamon method (Lu et al., 2005) were used to force the model.

Appendix B: Estimation of annual amplitude and phase

The TWS time series are represented by

$$L = f_0 + f_1 t + f_2 sin(\omega t) + f_3 cos(\omega t) + f_4 sin(2\omega t) + f_5 cos(2\omega t) \quad , \qquad \text{(B1)}$$

where L is the vector containing monthly TWS estimates, t is the observation time, and $\omega = 2\pi/T$ with T the annual period. The coefficients $f_0, \dots, f_5$ are estimated using least-squares adjustment. The annual amplitude (A) is estimated as

$$A = \sqrt{f_2^2 + f_3^2} \quad , \qquad \text{(B2)}$$

and the phase (φ) is estimated as

795 $\varphi = \arctan_2(f_2, f_3)$. (B3)

796 Note that the function $\arctan_2$ is realized in many high-level computer languages (e.g., function atan2 in

797 Matlab). The function always returns a value in the range $(-\pi, \pi]$.